JGR Atmospheres

RESEARCH ARTICLE
10.1029/2025JD045602

Anthropogenic Warming and Ocean Variability Exacerbated Spring 2024 Compound Floods in Central Asia

Mengyuan Yao[1,2], **Haosu Tang**[3], **and Gang Huang**[1,2]

[1]Key Laboratory of Earth System Numerical Modeling and Application, Institute of Atmospheric Physics, Chinese Academy of Sciences, Beijing, China, [2]University of Chinese Academy of Sciences, Beijing, China, [3]School of Geography and Planning, University of Sheffield, Sheffield, UK

Key Points:

- Spring 2024 saw the strongest compound flood in Northwestern Central Asia, with record-breaking precipitation and subsequent heatwave
- Current greenhouse gas-induced warming increased the likelihood of the 2024-like compound flood by eight times
- Cross-basin sea surface temperature anomalies contributed 31% to precipitation extremes and 68% to subsequent heatwaves

Supporting Information:

Supporting Information may be found in the online version of this article.

Correspondence to:

H. Tang and G. Huang,
haosu.tang@sheffield.ac.uk;
hg@mail.iap.ac.cn

Citation:

Yao, M., Tang, H., & Huang, G. (2026). Anthropogenic warming and ocean variability exacerbated spring 2024 compound floods in Central Asia. *Journal of Geophysical Research: Atmospheres*, *131*, e2025JD045602. https://doi.org/10.1029/2025JD045602

Received 8 OCT 2025
Accepted 20 FEB 2026

Author Contributions:

Conceptualization: Mengyuan Yao, Haosu Tang
Data curation: Mengyuan Yao
Formal analysis: Mengyuan Yao, Haosu Tang
Funding acquisition: Gang Huang
Investigation: Mengyuan Yao
Methodology: Mengyuan Yao, Haosu Tang
Project administration: Gang Huang
Resources: Mengyuan Yao
Software: Mengyuan Yao
Supervision: Haosu Tang, Gang Huang
Validation: Mengyuan Yao
Visualization: Mengyuan Yao
Writing – original draft: Mengyuan Yao
Writing – review & editing: Mengyuan Yao, Haosu Tang, Gang Huang

Abstract In spring 2024, northwestern Central Asia experienced catastrophic floods that displaced more than 100,000 people and caused severe socioeconomic disruption. This multi-peak compound disaster, marked by consecutive extreme precipitation and heatwaves, was the most devastating event since 1980. The March 3-day maximum precipitation (Rx3day) in 2024 exceeded its climatological mean by approximately threefold, while the April 7-day maximum temperature (Tx7day) exceeded the climatological average by 5.77 K. Using observations and climate model simulations, we show that anthropogenic warming increased the likelihood of 2024-like compound extremes, with greenhouse gases alone amplifying the risk by ~8-fold. Under a medium-emissions scenario (SSP2–4.5), this risk is projected to increase to more than 22-fold by the end of the twenty-first century. Sea surface temperature (SST) anomalies also play a critical role in shaping the consecutive rainfall and heat extreme events during 2024. An emerging Atlantic SST tripole, characterized by mid-latitude cooling, together with basin-wide Indian Ocean warming, enhances Rx3day through the increased westerly moisture transport, whereas a decaying La Niña tendency persisting from preceding winter to April favors persistent high-pressure anomalies and enhanced Tx7day. Linear decomposition indicates that internal variability reconstructed via SST anomalies explains approximately 31% and 68% of the observed anomalies in Rx3day and Tx7day, respectively, while external forcing acts primarily to amplify these extremes. Our results further highlight the importance of local thermodynamic feedback under ongoing global warming, which should be explicitly accounted for in projections of future regional compound floods.

Plain Language Summary Spring 2024 brought the most severe flooding in decades to Northwestern Central Asia. In late March, record-breaking precipitation occurred, with 3-day mean rainfall exceeding three times the climatological average. This was followed by extreme heat in April, when 7-day maximum temperatures were nearly 6°C above normal, forming a rare compound hydrometeorological event. Attribution analyses using Coupled Model Intercomparison Project Phase 6 (CMIP6) simulations indicate that greenhouse gas forcing increased the probability of such consecutive rainfall and heat extremes by approximately eightfold under current warming, with the risk projected to exceed a twentyfold increase by the end of the century. Internal climate variability also contributed significantly. An Atlantic tripole sea surface temperature pattern with mid-latitude cooling induced anomalous low pressure over Europe and high pressure over Siberia, enhancing westerly moisture transport and favoring extreme rainfall. By contrast, the April heatwave was primarily linked to a decaying La Niña from the preceding winter, which promoted persistent high-pressure and subsidence anomalies. Local land–atmosphere interactions, including soil moisture feedback, further modulated event intensity. These results indicate the combined roles of anthropogenic forcing, ocean-driven variability, and local feedback in shaping regional compound floods.

1. Introduction

Central Asia (CA), a vast and geographically diverse region comprising Kazakhstan, Turkmenistan, Kyrgyzstan, Uzbekistan, and Tajikistan, lies landlocked within the Eurasian continental interior. Characterized by its predominantly arid to semi-arid climate, the region features complex topography, scarce precipitation, high evaporation rates, and fragile ecosystems that are particularly sensitive to climate change (Fallah et al., 2024; Lioubimtseva & Henebry, 2009). Observational and modeling studies indicate that the frequency and magnitude of extreme weather events in CA show a dramatic increase under global warming, leading to more severe hazards such as floods, droughts, and landslides, as well as growing risks to public health and food security (Fallah et al., 2023; Tang et al., 2025; Tian et al., 2021; Yao, Li, et al., 2024). Specifically, extreme precipitation events

have become more intense and widespread in CA (K. Sun et al., 2025a, 2025b), while heatwaves are occurring more frequently, particularly across western and southern CA (Yao, Li, et al., 2024). In spring 2024, a devastating flood threatened the regions around northwestern CA (NWCA: 46–68°E, 46–56°N), drawing urgent attention from the Emergency Situations of Russia and Kazakhstan (Anna Chernova, 2024). The floods started on March 27, driven by a persistent rise in the Ural River's water levels, and peaked during its second wave in early April, causing extensive destruction and displacement of over 119,000 people, including 44,000 children (ACAPS, 2024; OCHA, 2024). Such multi-peak flood events, exacerbated by extreme atmospheric conditions, pose serious threats to mortality and water security (ACAPS, 2024; Guglielmi, 2022; Kurishbaev et al., 2024), underscoring the urgent need to identify and quantify the underlying driving mechanisms.

Radiative forcing changes, mainly driven by human activities, have significantly augmented the extreme events in CA (Fallah et al., 2023; Peng, Zhou, Zhang, & Zou, 2019; Peng et al., 2018; Zou et al., 2021). Specifically, global warming of 2°C has been linked to a ∼75% increase in moderate daily heat extremes, and a ∼40% increase in the frequency of daily precipitation extremes over land relative to pre-industrial levels, largely due to an accelerated hydrological cycle (Fischer & Knutti, 2015; Luo et al., 2019; Robinson et al., 2021) and modulated by meridional shifts of the subtropical westerly jet (SWJ) (Jiang & Zhou, 2021; Peng et al., 2018). In NWCA, particularly Kazakhstan, anthropogenic forcing is projected to substantially increase the likelihood of extreme precipitation and heat events, with a 3°C warming potentially increasing the risk of mudflows tenfold (Fallah et al., 2023; Fischer & Knutti, 2015; Peng, Zhou, Zhang, Zhang, & Chen, 2019). These changes are primarily driven by elevated greenhouse gas concentrations under anthropogenic forcing (Fallah et al., 2024; Peng, Zhou, Zhang, & Zou, 2019). However, previous studies mainly focus on the attribution of extreme trends in CA or individual extreme events in other regions (Fallah et al., 2023; Ito et al., 2023; Z. Wang et al., 2023; J. Xie et al., 2024), leaving the anthropogenic contribution to specific consecutive or compound extreme events less explored. The devastating 2024 NWCA flood highlights this gap in that the continuously rising water levels in the Ural River could be attributed to heavy precipitation and rapid snowmelt under pronounced warming and sustained high temperatures (Fallah et al., 2023; M. Zhang et al., 2017), ultimately triggering dam breaches, reservoir overflows, and large-scale population displacement. Although relatively rare, compound events—co-occurring or consecutive extremes—have become more frequent, spatially expansive, and exert far greater influences on human societies compared with individual events (Li et al., 2023; Tang et al., 2023; C. Wang et al., 2022).

In addition to anthropogenic forcing, internal climate variability—particularly sea surface temperature (SST) anomalies—can also modulate regional precipitation and temperature patterns in CA, contributing to their interannual and seasonal variability. Such SST anomalies could modulate both the strength and meridional displacement of SWJ, thereby altering large-scale moisture transport and ascent over CA (Umirbekov et al., 2022; Yao, Li, et al., 2024). Moreover, variability in the SWJ is linked to shifts in tropical convection and the Intertropical Convergence Zone (ITCZ), providing a pathway through which coupled tropical–extratropical interactions influence regional precipitation and temperature extremes (Stan et al., 2017). However, the influence of individual ocean basins and their interactions on atmospheric circulation over CA is highly complex and often difficult to disentangle. For instance, El Niño events tend to enhance precipitation over CA through large-scale convergence (Feng et al., 2022; Ren et al., 2025; Yao, Tang, et al., 2024). In contrast, North Atlantic tripole SST anomalies can trigger Rossby wave trains that interfere with this relationship, suppressing precipitation in CA (Ren et al., 2025; Yao, Tang, et al., 2024). Moreover, tropical Indian Ocean warming could induce a southward shift of SWJ via meridional circulation changes, thereby enhancing large-scale ascent in CA and moisture transport from the Arabian Sea (Meng et al., 2021; T. Xie et al., 2020). The Indian Ocean also plays a crucial role in modulating the South Asian jet stream and reinforcing the Pacific–North American (PNA) teleconnection pattern, thereby affecting Eurasian circulation patterns (Abid et al., 2021; Raganato et al., 2024). However, these signals may be masked by the dominant atmospheric response to El Niño during early winter (Abid et al., 2021; Raganato et al., 2024). Besides, decaying El Niño induces southwest Indian Ocean warming by triggering westward-propagating Rossby waves, which further amplifies North Indian Ocean warming through equatorially antisymmetric wind anomalies in spring and summer (Du et al., 2009; Wu et al., 2008; Yu et al., 2025). As for North Atlantic SST warming, it can trigger a teleconnection wave that enhances anticyclonic anomalies over CA, leading to extreme high-temperatures (X. Sun et al., 2019; Yao, Li, et al., 2024). On longer timescales, both Pacific decadal variability and the Atlantic Multidecadal Variability (AMV) have been identified as key drivers of interdecadal precipitation changes in CA (Jiang et al., 2021). A positive AMV phase potentially could weaken upper-level high-pressure systems over CA during summer, thereby alleviating extreme heat risks

(Dong et al., 2023), while enhancing barotropic high-pressure in winter and thus suppressing mean winter precipitation (Yao et al., 2025). Considering the influence of multiple ocean basins on atmospheric circulation over CA, we investigate how major tropical and mid-latitude SST anomaly patterns (TMSST; 10°S–80°N, 180°W–180°E) modulate the extreme events in NWCA, the core flood-affected region in spring 2024, through atmospheric teleconnection.

Detection and attribution (D&A) studies assess whether observed climate changes exceed internal variability and quantify the contributions of external forcings, particularly anthropogenic greenhouse gas emissions. Extending this framework, event attribution focuses on individual extremes to determine whether and to what extent human influence has altered their probability or intensity (Ito et al., 2023; Tang et al., 2023; Trenberth et al., 2015). Here, we examine the anthropogenic and natural drivers of the unprecedented compound precipitation–heatwave event that affected NWCA in spring 2024. Using observations together with the Coupled Model Intercomparison Project Phase 6 (CMIP6) climate model simulations, we apply a copula-based event attribution framework to quantify how anthropogenic forcing and internal circulation variability modulate the recurrence risk of 2024-like compound extremes. We further identify the dominant SST anomaly modes and elucidate the physical pathways through which they influence large-scale circulation and compound hazards over NWCA. Together, our results advance our understanding of future multi-hazard risks and provide a scientific basis for targeted mitigation and adaptation strategies in this highly climate-sensitive region.

2. Data and Methods

2.1. Data

To examine the extreme precipitation in March and heatwaves in April at daily to weekly scales, we use the daily precipitation and maximum/minimum temperature data sets from the Climate Prediction Center (CPC) global unified gauge-based analysis (Chen et al., 2008; T. Xie et al., 2010). Its reliability in NWCA has been confirmed by station observations from the Global Historical Climatology Network (GHCN) (W. Zhang et al., 2025). Daily mean temperature is obtained by averaging the maximum and minimum temperatures. We additionally incorporate daily precipitation from Multi-Source Weighted-Ensemble Precipitation (MSWEP) (Beck et al., 2019) and the fifth-generation European Center for Medium-Range Weather Forecasts atmospheric reanalysis (ERA5), together with daily surface air temperature from ERA5 (Hersbach et al., 2020). Meanwhile, atmospheric circulation fields are obtained from the ERA5 reanalysis, using post-processed daily statistics and monthly averages on pressure levels from 1940 to the present (Hersbach et al., 2020). Variables include SST, geopotential height, zonal and meridional winds, soil moisture, surface albedo and runoff. Additionally, monthly SST fields are derived from four observational and reanalysis products of Hadley Center Sea Ice and SST data set (HadISST) (Rayner et al., 2003), Extended reconstructed sea surface temperature (ERSST) version 5 (Huang et al., 2017), Optimum Interpolation Sea Surface Temperature (OISST) (Reynolds et al., 2007) and ERA5.

For event attribution, we use multi-model historical simulations and future projections of daily precipitation and surface air temperature from the Detection and Attribution Model Intercomparison Project (DAMIP) within the CMIP6 archive (Gillett et al., 2025). These include simulations forced by individual external forcings: greenhouse gases (hist-GHG; GHG), aerosols (hist-aer; AER), and natural factors (hist-nat; NAT). Historical simulations up to 2014 and future projections through 2100 under Shared Socioeconomic Pathways (SSP2–4.5) with all external forcings (hist-All; ALL) are also used. All simulations are extended beyond 2014 using corresponding SSP2–4.5 realizations. SSP2–4.5 represents a middle-of-the-road scenario, in which greenhouse gas emissions, aerosol forcing, and land-use changes are broadly aligned with many SSP-based integrated assessment model projections. Over the near-term period, differences among SSP scenarios are small relative to internal climate variability (Hawkins & Sutton, 2011). Consistent with this expectation, normalized Rx3day and Tx7day are examined using CMIP6 simulations under SSP1–2.6, SSP2–4.5, and SSP3–7.0 for the period 2022–2026, centered on the year 2024 (Figure S1 in Supporting Information S1). The close agreement across scenarios within this 5-year window indicates that the simulated near-term distributions of precipitation and heat extremes are largely insensitive to scenario choice, thereby supporting the robustness of our attribution results for the 2024 event. All CMIP6 models are equally weighted, irrespective of the number of realizations. All data are bilinearly interpolated to a $1° \times 1°$ grid for consistency. Model details are summarized in Table S1 of Supporting Information S1.

2.2. Tail Dependence Coefficient

To quantify the dependence structure between extreme wet and hot events beyond linear correlation, we employ the tail dependence coefficient, which measures the probability that one variable attains an extreme value conditional on the other variable also being extreme. Tail dependence provides a robust metric for characterizing the co-occurrence of extremes and is particularly relevant for compound event analysis. The lower tail dependence coefficient is defined as

$$\lambda_L = \lim_{q \to 0^+} P\left(Y \le F^{-1}_{\mathrm{Tx7day}}(q) | X \le F^{-1}_{\mathrm{Rx3day}}(q)\right) \tag{1}$$

which represents the asymptotic probability that Tx7day falls below its q-quantile given that Rx3day is simultaneously below its corresponding q-quantile. Similarly, the upper tail dependence coefficient is defined as

$$\lambda_U = \lim_{q \to 1^-} P\left(Y \ge F^{-1}_{\mathrm{Tx7day}}(q) | X \ge F^{-1}_{\mathrm{Rx3day}}(q)\right) \tag{2}$$

describing the probability that Tx7day exceeds its upper q-quantile conditional on Rx3day exceeding the same quantile level. Here, F_X^{-1} denotes the marginal quantile functions of variables X, respectively. Values of λ_U or λ_U close to zero indicate tail independence, whereas positive values imply non-negligible dependence in the extremes.

2.3. Joint Probability

Copulas are widely used to estimate the joint probability of multiple variables by coupling their marginal distributions while explicitly representing their dependence structure. Based on copula theory, the joint probability p of concurrent extreme precipitation and heatwave events can be expressed as

$$p(\mathrm{Precip} \ge x_1 \cap \mathrm{Temp} \ge x_2) = C_2\left[F_{\mathrm{Precip}}(x_1), F_{\mathrm{Temp}}(x_2)\right] \tag{3}$$

where x_1 and x_2 are the thresholds defining extreme precipitation and temperature, F_{Precip} and F_{Temp} are the corresponding marginal cumulative distribution functions, and C_2 is a bivariate copula function that maps the unit square $[0,1]^2$ to $[0,1]$ and encapsulates the dependence between the two extremes. To model joint extremes, we adopt a parametric copula framework in which the marginal and dependence structures are treated separately. The univariate tails of Rx3day and Tx7day are modeled using the Generalized Extreme Value (GEV) distribution, fitted to annual block maxima to characterize precipitation and temperature extremes. The fitted GEV marginal distributions are then coupled using a bivariate t-copula to estimate joint exceedance probabilities. As both the lower and upper tail dependence coefficients are approximately zero in the near-term period (2022–2026) but 0.17 during the far-future period (2075–2099) under the ALL and GHG scenarios, the dependence structure between extreme precipitation and heat exhibits weak but non-negligible tail dependence in the far-future period. To account for this feature, a t-copula is adopted, as it allows for symmetric tail dependence while retaining flexibility in representing moderate correlations.

To quantify the anthropogenic influence, we calculate the risk ratio (RR), defined as the fraction p_a/p_{NAT} (with a $=$ GHG, AER, ALL). An RR > 1 indicates an increased likelihood of spring 2024-like flood events under different anthropogenic forcings relative to natural conditions. Given the sampling uncertainty and temporal dependence in the extreme indices, a block bootstrap approach is performed with 1,000 iterations to estimate the mean RR and its 5th–95th percentile confidence interval (CI) (Künsch, 1993; Min et al., 2022; Tang et al., 2023). Contiguous blocks are resampled with replacement to preserve serial persistence in the time series. The block length is objectively determined based on the temporal autocorrelation structure of the data. Specifically, block length is defined as the lag at which the autocorrelation function (ACF) first decays to 1/e based on the CMIP6 multi-model ensemble mean (MME) time series. According to this criterion, the estimated block lengths for the 2022–2099 period are 15 years for Rx3day and 6 years for Tx7day. To assess sensitivity to the choice of block length, we repeat the bootstrap analysis using block sizes of 13, 15, and 17 years for Rx3day, and 5, 6, and 7 years for Tx7day. The resulting RR estimates are highly consistent across these choices, indicating that the attribution results are robust to reasonable assumptions about temporal dependence.

2.4. Reconstruction of Extreme Event Indices

Our preliminary analysis indicates that the linear trends of TMSST, the extreme precipitation index (Rx3day), and the extreme heatwave index (Tx7day) reflect the long-term response to global warming. To isolate the influence of internal variability expressed by large-scale SST anomalies from this warming trend, we first linearly detrend the extreme indices (Rx3day in May and Tx7day in April) and their simultaneous TMSST. Meanwhile, the 9-year running mean is removed from TMSST to eliminate the influence of decadal variability. Next, grid-point linear regressions of the detrended TMSST(t, i, j) anomalies are regressed onto the detrended Rx3day and Tx7day indices based on the partial least squares (PLS) method, where t denotes year and (i, j) are spatial grids. PLS regression is adopted here because it explicitly extracts predictor patterns that maximize the variance of a predefined predictand, rather than merely maximizing covariance or correlation between two fields (Abdi, 2010; Smoliak et al., 2010). This property makes PLS particularly well suited for diagnosing the modulation effect of large-scale SST variability on extreme event indices, which has been successfully applied in previous studies to identify physically interpretable oceanic drivers (Hu et al., 2020; Smoliak et al., 2010; Wallace et al., 2012). The resulting regression coefficient fields are referred to as Mode1 for Rx3day and Tx7day, respectively, representing the leading SST patterns associated with extreme precipitation and heatwave variability over NWCA. By construction, these modes correspond to SST anomaly structures whose temporal evolution explains the largest fraction of variance in the respective extreme indices, and thus represent the dominant SST-related modulation pathways. To extract the temporal evolution of these modes, the detrended TMSST field is regressed onto Mode1, yielding the corresponding principal component time series (PC1) for Rx3day and Tx7day. These PC1s describe the temporal evolution of the leading SST modes that modulate Rx3day and Tx7day, respectively.

To identify additional, independent SST influences, the SST components associated with PC1 are removed from the detrended TMSST field, and their corresponding contributions are simultaneously subtracted from the extreme indices. This procedure yields residual SST fields and residual extreme indices, ensuring that subsequent modes capture independent modulation signals rather than being contaminated by previously extracted dominant patterns. The above steps are then repeated iteratively on the residuals to obtain higher-order SST modes (Mode2, Mode3, etc.) and their associated time series (PC2, PC3, etc.), until additional modes explain only negligible variance in the extreme indices.

Following the iterative extraction of TMSST modes, we select only those that (a) exhibit physically interpretable spatial patterns, and (b) are significantly correlated with the detrended extreme indices at the 95% confidence level. The detrended extreme indices are then reconstructed as linear combinations of the selected SST mode time series, representing the portion of variability attributable to SST-driven processes. The statistical separability between the long-term trend and SST-driven internal variability is therefore permitted by the fact that the selected SST modes are both mutually independent and trend-free over the analysis period.

2.5. Leave-Three-Out Cross-Validation and Independent Prediction

Before determining the number of PCs to be used for reconstructing the extreme indices, we first assess the mutual independence of the candidate PCs using Pearson correlation coefficients. In addition, the variance inflation factor (VIF) is employed to diagnose potential multicollinearity among PCs within the regression framework, as strong collinearity can inflate regression coefficients and weaken model robustness. The VIF is defined as

$$\mathrm{VIF} = 1 / \left(1 - r^2\right) \tag{4}$$

where r denotes the multiple correlation coefficient between a given PC and the remaining PCs included in the regression model. A VIF value close to 1 indicates negligible multicollinearity, whereas larger values imply increasing redundancy and reduced statistical reliability.

To assess the robustness and predictive skill of the statistical reconstruction models, a Leave-three-out cross-validation was employed during the training period of 1980–2010. In each iteration, consecutive 3 years are excluded from the training data set, and the regression model is built using the remaining years. The excluded year is then reconstructed using the fitted model, yielding a cross-validated estimate. This procedure is repeated sequentially for all years in the training period, ensuring that each reconstructed value is based on a model trained without that year. Model performance is evaluated using the Pearson correlation coefficient and the root mean

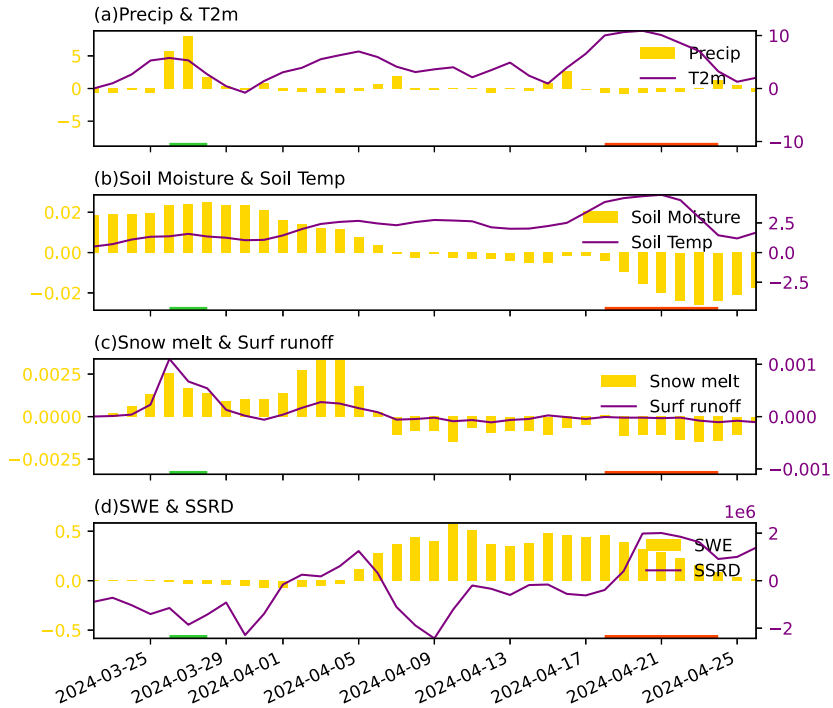

Figure 1. Time evolution of (a) precipitation (unit: mm day^{-1}) and surface temperature (unit: K) over the NWCA region (46–68°E, 46–56°N) (a) 0–7 cm soil moisture anomalies (unit: m^3 m^{-3}) and soil temperature anomalies (unit: K), (b) snowmelt anomalies (unit: m) and surface runoff anomalies (unit: m), and (c) snow water equivalent (SWE) anomalies (unit: kg m^{-2}) and surface solar radiation downwards (SSRD) anomalies (unit: m). The green and red horizontal lines mark the occurrences of Rx3day and Tx7day, respectively.

square error (RMSE) between the reconstructed and observed indices. To further test the temporal generalizability of the models, an independent prediction was conducted for the period 2011–2024 using regression coefficients derived solely from the 1980 to 2010 training period.

2.6. Climate Indices Definition

To characterize large-scale SST variability relevant to precipitation and temperature extremes over NWCA, we employ several widely used SST–based climate indices. The Indian Ocean Dipole (IOD) index is defined as the area-averaged SST difference between the western equatorial Indian Ocean (50–70°E, 10°S–10°N) and the southeastern equatorial Indian Ocean (90–110°E, 10°S–0°). The Indian Ocean Basin Mode (IOBM) is defined as the leading empirical orthogonal function (EOF) mode of SST anomalies over the Indian Ocean domain (40–110°E, 20°S–20°N), representing basin-wide coherent SST variability. In addition, the Niño3.4 index is calculated as the area-averaged SST anomaly over the central equatorial Pacific (5°S–5°N, 170°–120°W) and is used to characterize ENSO-related variability.

Guided by the leading coupled SST modes associated with Rx3day and Tx7day, we further define the regional Atlantic and Pacific indices. The March Atlantic Index (MAI) is defined as the difference between the area-averaged SST in March over the high- and low-latitude Atlantic (60°W–30°W, 45°–60°N and 50°W–15°W, 5°–20°N) and the mid-latitude North Atlantic (80°W–40°W, 25°–40°N) (magenta boxes in Figure 4a), while April Atlantic Index (AAI) is calculated as the area-averaged SST in April over the mid-latitude North Atlantic (50°W–25°W, 25°–45°N) minus the mean SST averaged over two adjacent regions (45°W–15°W, 5°–20°N and 55°W–30°W, 50°–65°N) (magenta boxes in Figure 4b).

At interdecadal timescales, the Pacific Decadal Oscillation (PDO) index is defined as the leading EOF of monthly SST anomalies over the North Pacific (20°–70°N). Prior to EOF analysis, the global mean SST anomaly was removed.

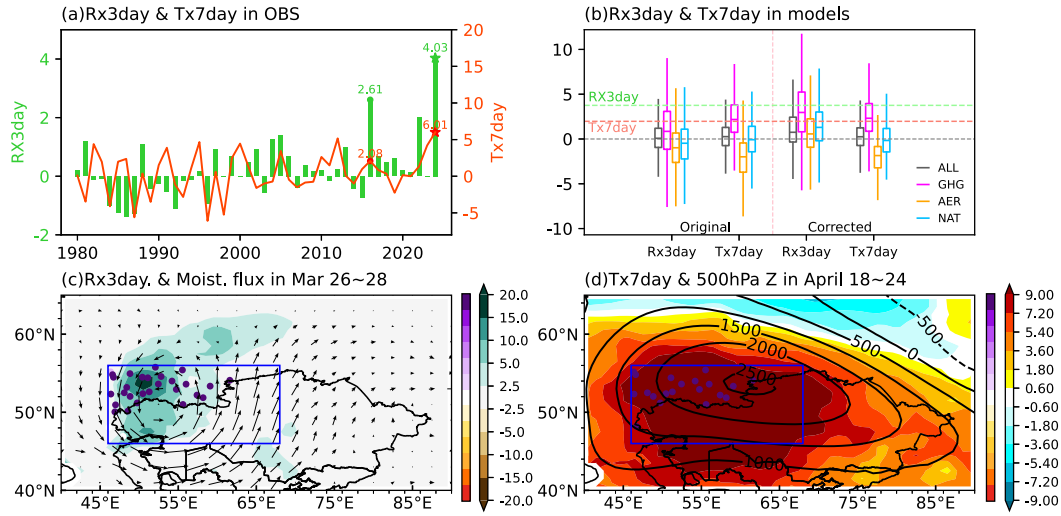

Figure 2. (a) Observed time series of areal averaged Rx3day (units: mm day^{-1}) in March and Tx7day (units: K) in April over the NWCA region (46–68°E, 46–56°N) based on CPC data sets during 1980–2024. (b) Quartile boxplots of normalized Rx3day and Tx7day from CMIP6 (ALL, GHG, NAT, and AER forcings) original and corrected model simulations during 1980–2024. The error bars denote the 5th–95th percentile range of simulations across model ensemble members. Dashed lines indicate the thresholds defined as the 2024 observations, with green for Rx3day and pink for Tx7day. (c) Anomalous Rx3day (units: mm day^{-1}; shading) and 850-hPa moisture flux (units: kg m^{-1} Pa^{-1} s^{-1}; vector) during 26–28 March 2024, and (d) Anomalous Tx7day (units: °C; shading) and 500-hPa geopotential height (units: m; contour) during 18–24 April 2024, relative to the 1980–2010 climatology. The dots represent the station observations from GHCN. Blue boxes in (c) and (d) indicate the NWCA region affected by the spring 2024 flood.

3. Results

3.1. Observed Characteristics and Model Evaluation of the 2024 Wet–Hot Compound Event

The spring 2024 floods over NWCA began on 27 March and peaked in early April, driven by heavy precipitation followed by elevated temperatures that accelerated snowmelt and runoff (Fallah et al., 2023; M. Zhang et al., 2017). Relative to the 1980–2010 baseline, pronounced precipitation anomalies over NWCA emerged on 26 March 2024, exceeding 5.8 mm day^{-1} and persisting for three consecutive days, while a subsequent heatwave with surface air temperature anomalies exceeding 7 K occurred from 18 to 23 April (Figure 1a). To objectively characterize these extremes, we assessed grid-point exceedances of the 90th percentile threshold for daily precipitation and surface air temperature across NWCA. This analysis identifies three dominant heavy precipitation days in March and seven heatwave days in April (Figures S2a and S2b in Supporting Information S1). Accordingly, extreme precipitation index (Rx3day) is defined as the maximum 3-day averaged precipitation in March, and the extreme heatwave index (Tx7day) as the mean surface air temperature over seven consecutive days in April. These indices have been widely used in previous event attribution studies (W. Zhang et al., 2020; Zhou et al., 2021). Both indices reach their highest values since 1980 (Figure 2a). Rx3day exceeds the climatological mean of 1.81 mm by more than threefold, reaching 5.85 mm, while Tx7day surpasses the climatological average of 12.63 K by 5.77 K. The successive wet–hot event in 2024 is therefore unprecedented in the historical records with return periods based on GEV fitting of 273 years [CI: 46–495 years] for Rx3day and 139 years [CI: 43–250 years] for Tx7day, and no comparable compound extremes of similar magnitude. Physically, enhanced surface soil moisture and rapid snowmelt during March 2024 intensify the precipitation–runoff response during the Rx3day event (Figure 1). Following the precipitation peak, accelerated soil drying and sustained soil warming suppressed evaporative and snow-surface cooling, allowing stronger shortwave radiative heating to amplify the subsequent Tx7day heatwave. Such flood–heat compound extremes substantially increase post-disaster recovery costs and markedly elevate the risks of heat stress and heat-related mortality (Blum et al., 2024; Liang et al., 2024; Rahman et al., 2024). For comparison, all analyses are further repeated using 2016 observations, the second most severe compound event based on the joint probability of March Rx3day and April Tx7day (Figure S2c in Supporting Information S1). In 2016, Rx3day and Tx7day exceeded climatology by 2.61 mm day^{-1} and 2.08°C, respectively (Figure 1a).

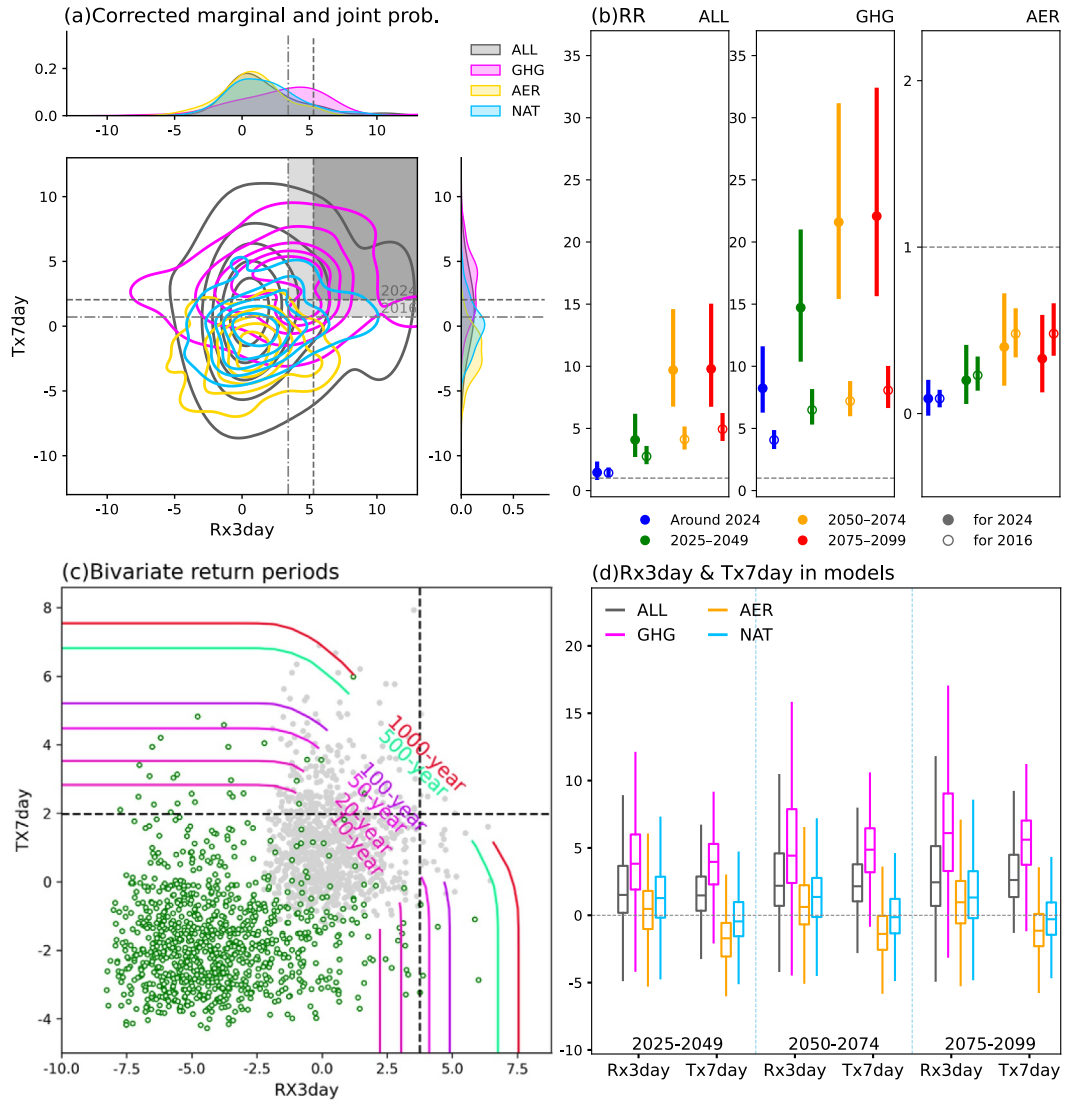

Figure 3. (a) Marginal and joint probability distributions of normalized corrected Rx3day and Tx7day from CMIP6 (ALL, GHG, NAT, and AER forcings) under the SSP2–4.5 scenario during 2022–2026. Dashed and dotted lines indicate the 2024 and 2016 thresholds, respectively. (b) RR of compound floods under ALL, GHG, and AER forcings relative to NAT forcing, based on 2024 (left; solid circles and thick bars) and 2016 (right; hollow circles and thin bars) thresholds. Circles and error bars indicate the averages and 5%–95% CI ranges of the corresponding RR. As the error bars of RR for ALL and GHG in 2016 are too short to show, their ranges are displayed under the corresponding axes. (c) Bivariate return periods of the compound event (units: mm day^{-1} and °C) under ALL (contours and gray scatters) and NAT forcings (green scatters). The vertical (horizontal) dashed line indicates the threshold of Rx3day (Tx7day) in model simulations. (d) Quartile boxplots of normalized corrected Rx3day and Tx7day in CMIP6 models (ALL, GHG, NAT, and AER forcings) for the near future (2025–2049), mid-century (2050–2074), and late-century (2075–2099) periods. The error bars denote the 5th–95th percentile range of projections across model ensemble members.

Additionally, we further evaluated the robustness of our results using higher spatial resolution data (0.5° × 0.5°), alternative observational data sets, including MSWEP and ERA5, as well as alternative index definitions. Both the temporal evolution and spatial patterns of Rx3day and Tx7day derived from the CPC data set at 0.5° × 0.5° resolution remain highly consistent with those at 1° × 1° (Figures S3a and S3b in Supporting Information S1). For 2024, Rx3day reaches 5.86 mm day^{-1} and Tx7day 19.07°C at 0.5° × 0.5°, compared with 5.86 mm day^{-1} and 18.65°C at 1° × 1°, indicating that the differences induced by spatial resolution are negligible. Besides, the sensitivity analysis includes longer averaging windows (Rx5day, Rx7day, Tx3day, and Tx5day) and percentile-based thresholds for March daily precipitation (R95th, R99th) and April temperature (T95th, T99th). Across all

data sets and index definitions, the resulting time series and spatial patterns are perfectly related with those derived from CPC observations ($p < 0.001$), consistently identifying 2024 as the most extreme compound wet–hot event on record. This strong agreement confirms that the unprecedented magnitude of the 2024 Rx3day and Tx7day anomalies is highly robust (Figure S3 in Supporting Information S1). Note that although the correlation coefficients between March Rx3day and April Tx7day are statistically insignificant ($p > 0.05$) in both observations and climate models, implying that such consecutive wet–heatwave events could be regarded as largely random occurrences, this lack of linear correlation does not imply full independence. Rather, antecedent hydrological and land-surface conditions provide a physical linkage between the two extremes. Beyond hydrological linkages, compound humid–heat extremes can impose disproportionately larger impacts on human and socio-ecological systems than wet or hot extremes alone, by amplifying heat stress on human health and agricultural systems (Blum et al., 2024; Liang et al., 2024; Rahman et al., 2024).

To ensure comparability between models and observations, the Rx3day and Tx7day indices are normalized as percentage anomalies relative to the climatology (1980–2010 mean) in the model simulations. For attribution experiments, simulations under GHG, NAT, and AER forcings are normalized using the ALL-forced climatology of each model. Before conducting attribution analysis, the performance of models in simulating Rx3day and Tx7day in NWCA is first assessed. CMIP6 models reasonably capture the climatological spatial pattern of Rx3day, characterized by increasing intensity toward NWCA, and Tx7day, which follows a latitudinal gradient, weakening northward (Figure S4 and Table S1 in Supporting Information S1). Meanwhile, the historical model simulations were able to reproduce the observed Rx3day and Tx7day variability during 1980–2014 (Figure S5 in Supporting Information S1).

Although models can reasonably simulate individual extremes, they often fail to reproduce the magnitude of successive extreme events. This limitation complicates the attribution of compound extreme events within the traditional framework and hinders the reliable estimation of RR (J. Wang et al., 2022; Z. Wang et al., 2023). Compound floods in the downstream Ural River may arise not only from localized heavy precipitation and snowmelt caused by rapid warming but also from remote drivers such as intense upstream precipitation. To better reconcile these processes in models, a sliding reference zone is considered for model magnitude adjustment. Specifically, a rectangular box (Figure S2a in Supporting Information S1, solid box: 46–68°E, 46–56°N) of fixed size and grid count is allowed to shift within a broader domain (Figure S1a in Supporting Information S1, dashed box: 45–75°E, 45–65°N) at each time step. For each model and time step, the maximum value within the sliding box is recorded as the extreme index, and the corresponding area is defined as the attribution zone. This correction approach, successfully applied in previous studies (Z. Wang et al., 2023), could enhance the model's ability to capture event magnitudes.

Both the original and corrected model simulations confirm the rarity of events exceeding the absolute or relative thresholds, whether considered as single or joint extremes (Figure 2b). During spring 2024, much of NWCA experienced extremely wet and hot conditions, which is also represented by observational records from GHCN with valid records for precipitation in March 26–28 and surface temperature in April 18–24 (Figures 2c and 2d). The consecutive precipitation from March 26 to 28 occurred over climatologically high precipitation regions, effectively amplifying the seasonal wet signal (Figure 2c and Figure S4c in Supporting Information S1). By contrast, the extreme temperature anomalies from April 18 to 24 emerge through a local breakdown of the climatological latitudinal temperature gradient, driven by anomalous atmospheric circulation and amplified by local soil moisture–temperature feedbacks (Figure 2d and Figure S4d in Supporting Information S1). Atmospheric circulation anomalies provided favorable conditions for these successive extremes: a cyclonic low-level moisture convergence anomaly from March 26 to 28 supplied abundant moisture for sustained precipitation (Figure 2c), followed by anomalous mid-level high pressure from April 18 to 24, which favored shortwave reaching radiation and adiabatic warming, intensifying the surface heatwave (Figure 2d).

3.2. The Role of External Forcing on Rx3day and Tx7day

Influences of diverse external forcings on the likelihood of the 2024-like March Rx3day and April Tx7day events in historical records (1980–2024) are investigated in Figure 2b. Based on the corrected simulations, aerosol (AER) forcing contributes far less or even offsets the humidification and warming induced by GHGs, while natural variability slightly enhances Rx3day but has little impact on Tx7day (Figure 2b, right cell), as further confirmed by the marginal probability in Figure 3a. Original model outputs yield consistent results, albeit with

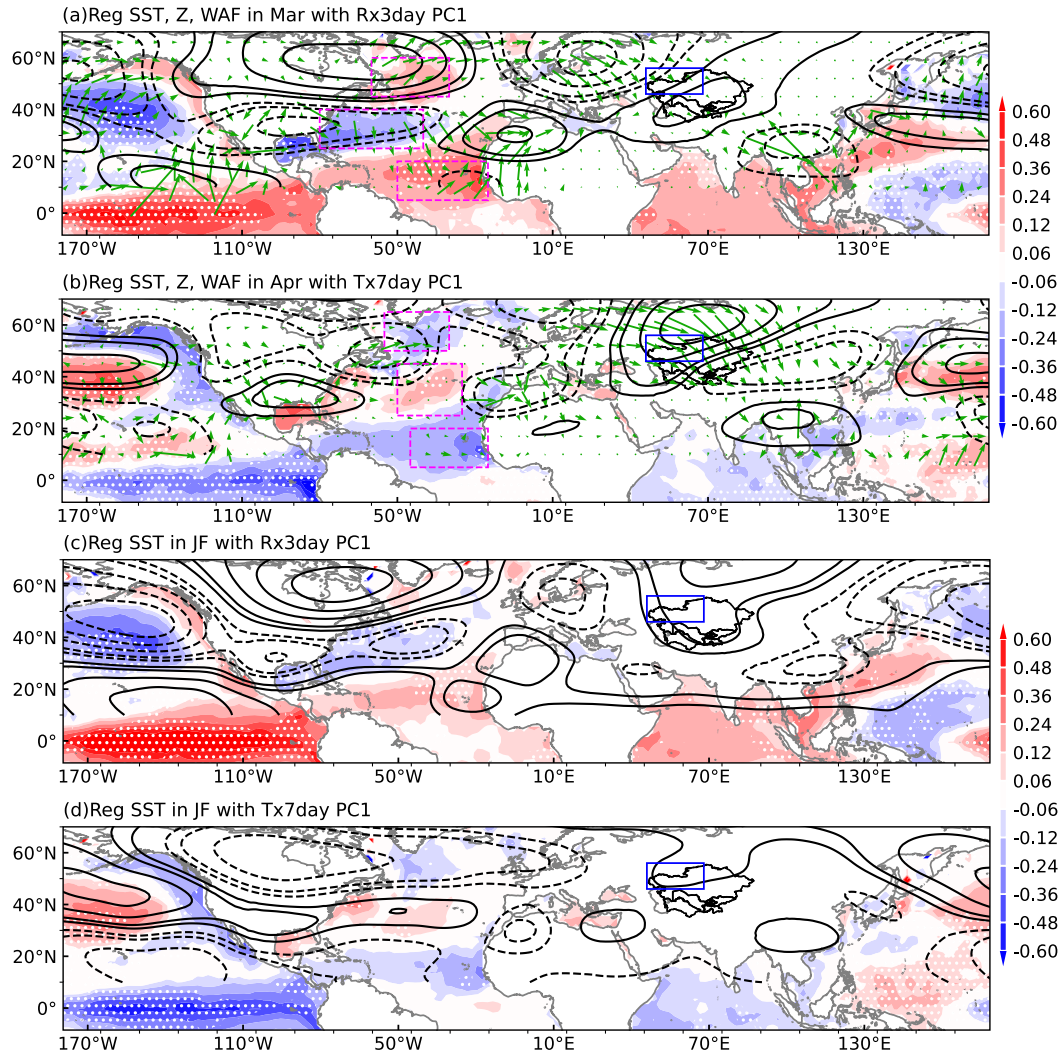

Figure 4. Regression of detrended SST (unit: K), 200-hPa geopotential height (shading; units: m) and corresponding wave activity fluxes (vectors; units: 10^{-2} m^2 s^{-2}) onto PC1 of (a) Rx3day in March and (b) Tx7day in April. The magenta boxes indicate the regions for MAI and AAI index. (c, d) Same as (a, b), but for January–December. Dotted areas indicate regions significant at the 90% confidence level based on the Granger causality test (Sun et al., 2025b).

larger uncertainty ranges (Figure 2b, left cell). Joint probability analyses demonstrate that GHG forcing favors the succession of heavy precipitation and heatwave events in both 2024 and 2016, whereas AER acts as a negative contributor (Figure 3a). Quantitatively, CMIP6 results indicate that the probabilities of 2024-like consecutive extremes (P_{ALL}, P_{GHG}, P_{AER}, and P_{NAT}) are 5.10%, 28.80%, 0.30%, and 3.50%, respectively, for the 5-year period centered on 2024. The corresponding $RR_{ALL/NAT}$, $RR_{GHG/NAT}$, and $RR_{AER/NAT}$ are 1.46 [CI 1.02, 2.71], 8.23 [CI 6.44, 11.44], and 0.09 [CI 0.00, 0.19], respectively (Table 1). These results imply that human activities have increased the risk of 2024 record-breaking compound extremes, with GHG emissions alone responsible for an 8-fold amplification (Figure 3b). In addition, the 2024-like compound event is virtually unlikely to occur under natural forcings alone, with low-amplitude fluctuations of the return period in the Rx3day and Tx7day. Under external forcing, however, their recurrence risk rises to nearly once in 100 years (Figure 3c).

We further examine the role of anthropogenic forcing in the near future (2025–2049), mid-century (2050–2074), and late 21st century (2075–2099) (Figure 3d, Table S2 in Supporting Information S1). The response of Rx3day and subsequent Tx7day to anthropogenic GHG forcing gradually intensifies over time, reaching its peak in the late 21st century, when both indices increase in tandem with larger associated uncertainties, consistent with previous studies (Fallah et al., 2023; Fischer & Knutti, 2015). The RR of exceeding the 2024 thresholds reaches

Table 1
Probability and RR Values of Single Rx3day and Tx7day and Their Co-Occurrence Exceeding the Corresponding Percentile Thresholds of 2024 and 2016 During 2022–2026

	Variables	Prob. of ALL	Prob. of GHG	Prob. of AER	Prob. of NAT	RR of ALL	RR of GHG	RR of AER
2024	Rx3day	12.70%	40.40%	7.60%	14.00%	0.91 [0.76, 1.10]	2.89 [2.51, 3.35]	0.54 [0.43, 0.68]
	Tx7day	27.60%	63.20%	0.40%	13.90%	1.99 [1.72, 2.34]	4.55 [4.09, 5.28]	0.03 [0.01, 0.06]
	Co-occurrence	5.10%	28.80%	0.30%	3.50%	1.46 [1.02, 2.17]	8.23 [6.44, 11.44]	0.09 [0.00, 0.19]
2016	Rx3day	24.80%	62.00%	15.40%	30.70%	0.81 [0.71, 0.91]	2.02 [1.82, 2.21]	0.50 [0.43, 0.57]
	Tx7day	67.80%	85.20%	5.60%	31.00%	2.19 [2.02, 2.37]	2.75 [2.55, 2.96]	0.18 [0.14, 0.22]
	Co-occurrence	19.00%	54.50%	1.20%	13.40%	1.42 [1.19, 1.69]	4.07 [3.51, 4.70]	0.09 [0.05, 0.13]

Note. Parentheses indicate 5%–95% uncertainty ranges of RR estimated by the Monte Carlo bootstrap method.

9.79 [CI 6.91, 14.87] by the late 21st century, exceeds double the near-future value of 4.08 [CI 2.87, 6.01] and approximately double compared to the 2016 thresholds. AER forcing consistently weakens the risk of extreme events (RR < 1), while the response to NAT forcing remains wetting for Rx3day and cooling for Tx7day (Figure 3d). For univariate extremes, GHG forcing amplifies the risk of both extreme precipitation and high temperatures, with RRs of 3.21 [CI 2.77, 3.65] for Rx3day and 5.82 [CI 5.16, 6.57] for Tx7day in the near future. Comparing univariate and bivariate extremes across decades reveals that the risk of joint events is substantially higher under GHG or ALL forcings. Notably, the unprecedented 2024-like compound extremes exhibit a far greater amplification than that in 2016, underscoring that the more severe the event, the larger the associated RR (Table S2 in Supporting Information S1). In addition, sensitivity analyses are based on two additional sets of extreme indices, Rx5day and Tx5day, as well as percentile-based indices R95th and T95th. The resulting RR estimates consistently support the conclusion that anthropogenic forcing increases the likelihood of extreme events, with GHG exerting a stronger amplifying effect, particularly toward the far-future period (Table S3 in Supporting Information S1).

3.3. Mechanisms of SST Anomalies Modulating Compound Extremes

To further elucidate the role of internal climate variability in modulating precipitation and temperature extremes over NWCA, we removed the long-term linear trend from the tropical–midlatitude SST (TMSST) field at each grid point and extracted the leading detrended SST modes that are significantly associated with Rx3day and Tx7day, together with their corresponding temporal components (Figures 4 and 5). Lead-lag regression and Granger-causality diagnostics indicate that these SST modes precede and exert a statistically significant influence on the extreme indices, supporting a physically interpretable causal linkage. The leading SST mode associated with detrended Rx3day is characterized by a decaying El Niño pattern accompanied by a developing Atlantic SST dipole from preceding winter (January–February) to March, featuring midlatitude cooling flanked by subtropical and high-latitude warming, together with basin-wide warming over the Indian Ocean (Figures 4a and 4c). The corresponding PC1 exhibits significant correlations with the Niño3.4 (r = 0.64), MAI (r = 0.57), and IOBM (r = 0.65) indices, which could be traced back to the preceding winter with seasonal persistence. Consistent with previous studies, Niño3.4 and IOBM are strongly correlated (r = 0.66), supporting the role of the Indian Ocean Basin Mode as a "capacitor" that stores and prolongs ENSO-related signals (J. Yang et al., 2007; Y. Yang et al., 2015). Collectively, this SST mode explains 38% of the internal variability in detrended Rx3day. The associated atmospheric response is characterized by an eastward-propagating barotropic wave train originating in the preceding winter, with anomalous low pressure over Europe and high pressure over Siberia in March (Figures 4a and 4c). This circulation pattern is primarily modulated by the Atlantic SST tripole, which strengthens the SWJ over NWCA and enhances zonal moisture transport from the Atlantic, thereby intensifying Rx3day extremes. Meanwhile, the pure Indian Ocean basin-wide warming after removing the Niño3.4 signal tends to amplify the anomalous high pressure over NWCA, favorable for Rx3day (Figures S6a–S6c in Supporting Information S1). At the regional scale, anomalous moisture fluxes during Rx3day are dominated by westerly transport, while southerly moisture transport anomalies from the southern Indian Ocean contribute preferentially to precipitation over the eastern NWCA. Notably, surface soil moisture anomalies in March did not emerge as a significant precursor or controlling factor for Rx3day variability (Figures 5a–5c).

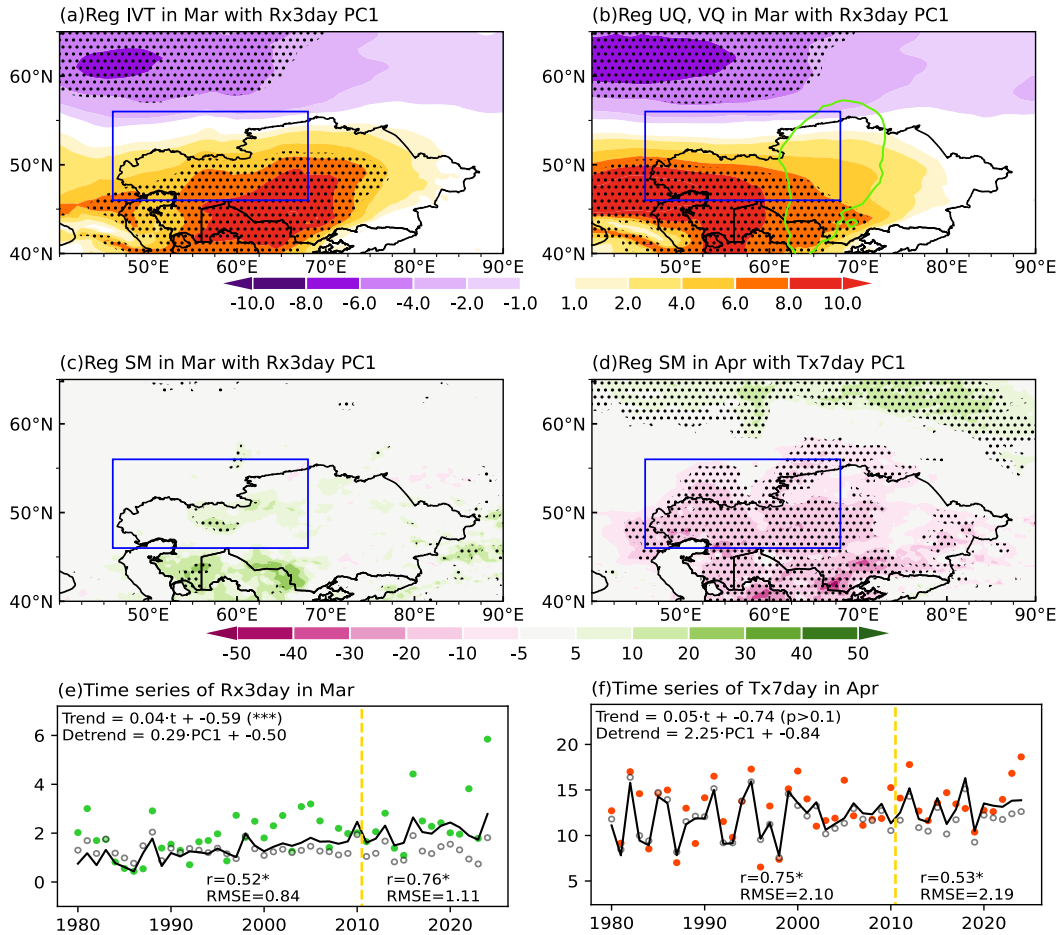

Figure 5. Regression of (a) vertically integrated horizontal moisture transport (IVT; unit: kg m^{-1} s^{-1}), (b) zonal (shading; unit: kg m^{-1} s^{-1}) and meridional moisture transport (green contours of 5 kg m^{-1} s^{-1}), and (c) soil moisture (units: mm) onto Rx3day PC1 in March. (d) Same as (c), but for Tx7day PC1 in April. (e, f) Time series of observation, reconstruction, and trends of Rx3day and Tx7day. Yellow dashed lines indicate the year 2011. Asterisks denote correlations statistically significant at the 90% confidence level.

On the other hand, detrended Tx7day is primarily associated with a decaying La Niña pattern from the preceding winter, concurrent with an emerging Atlantic SST tripole characterized by midlatitude cooling and subtropical and high-latitude warming. The Tx7day PC1 exhibits significant correlations with Niño3.4 ($r = -0.39$) and AAI ($r = 0.46$), together accounting for 59% of the internal variability in detrended Tx7day (Figures 4b and 4d). The circulation anomalies associated with Tx7day PC1 favor strengthened high-pressure anomalies and enhanced subsidence over NWCA. However, contributions from Niño3.4 and the AAI alone cannot fully account for the strong and persistent anticyclonic anomalies dominating CA (Figures S6d–S6f in Supporting Information S1). Instead, the decay tendency of La Niña, defined as the difference in the inverted Niño3.4 index between April and the preceding January–February, plays a leading role in intensifying surface solar radiation and sustaining prolonged heat extremes (Figures S6d–S6f in Supporting Information S1). At the local scale, elevated geopotential heights and enhanced solar radiation promote soil moisture depletion, intensifying sensible heat fluxes and amplifying extreme heat through land–atmosphere feedbacks (Figure 5d). These SST-based dominant modes are robust across alternative SST data sets (OISST, ERSST and ERA5) and remain robust to the choice of running window length (11 years) and detrending strategy, including quadratic detrending (Figure S7 in Supporting Information S1).

The reconstruction of detrended Rx3day and Tx7day indices using PCs is predicated on the selection of modes that (a) explain sufficient variability independent of the long-term linear trend, (b) are mutually orthogonal, and (c) exhibit significant correlations with the corresponding extreme indices (Tables S4–S6 in Supporting

Information S1). Specifically, detrended Rx3day shows a significant correlation of 0.60 with its leading PC1, while detrended Tx7day displays a correlation coefficient of 0.75 with its PC1. Importantly, these PC1s are statistically independent of the long-term trends of the corresponding extreme indices (Table S4 in Supporting Information S1). Although the remaining modes are orthogonal and introduce negligible increases in VIFs, their inclusion provides little additional predictive skill for detrended Rx3day and Tx7day (Tables S4–S6 in Supporting Information S1). Accordingly, linear regression models are constructed using only the first standardized PC for each index.

For Rx3day, the best-fit model is given by $detrended\ Rx3day = 0.29 \times \mathrm{PC1} - 0.50$, combined with a linear trend term of $0.04 \times t - 0.59$, where t ranges from 1 to 45, corresponding to 1980–2024. These two statistically separable components are combined to yield the full reconstruction. Under leave-three-out cross-validation, the reconstructed Rx3day reproduces observations, with a correlation coefficient of 0.52 and an RMSE of 0.84 (Figure 5e). During the independent prediction period (2011–2024), model skill improved, yielding a correlation of 0.76 and an RMSE of 1.11. For the year 2024, the long-term trend contributes 17% (90% confidence interval: 2%–34%) of the Rx3day amplitude, while SST-related internal variability accounts for 31%. In parallel, the Tx7day index is reconstructed with detrended $\mathrm{Tx7day} = 2.25 \times \mathrm{PC1} - 0.84$, plus a linear trend term of $0.05 \times t - 0.74$. This model reproduces observations with high skill, achieving a correlation of 0.75 and an RMSE of 2.10 under leave-three-out cross-validation (Figure 5f). During the independent prediction period, the reconstruction attains a correlation of 0.53 with an RMSE of 2.19. For the 2024 event, Tx7day is primarily attributable to internal circulation anomalies linked to SST variability (68%), with an additional contribution of 8% from long-term warming (90% confidence interval: −7%–24%). Notably, even after statistical reconstruction, the compound wet–hot extremes in 2024 over NWCA remain the most exceptional anomalies on record since 1980 (Figure S2c in Supporting Information S1). This highlights internal climate variability playing a non-negligible role, accompanied by the extreme amplification forced by externally forced warming.

4. Conclusion and Discussion

The unprecedented spring 2024 flood NWCA caused widespread socio-economic disruption and displaced over 100,000 people. This extreme compound event is characterized by consecutive hazards of an anomalous heavy precipitation episode (Rx3day) in March, followed by an intense heatwave (Tx7day) in April. Such back-to-back extremes in NWCA offer a unique opportunity to disentangle the extent to which regionally amplified compound events in NWCA are contributed by externally forced global warming versus internal climate variability, particularly circulation anomalies? Leveraging both observations and climate model simulations, we quantify the relative contributions of anthropogenic warming and internal atmospheric dynamics to the unprecedented spring 2024 compound wet–hot extremes over NWCA. Our findings reveal that the consecutive Rx3day and Tx7day events in spring 2024 are the most extreme since 1980, Rx3day exceeds the climatological mean by more than a factor of three, reaching 5.85 mm, while Tx7day surpasses the climatological average by 5.77 K. Moreover, we identify the dominant anomalous SST modes modulating these extremes and elucidate the underlying dynamical mechanisms.

To address model limitations in capturing compound extremes, we first define events based on percentile anomalies over a sliding reference area to identify spatially aligned extremes. Attribution analysis using CMIP6 DAMIP simulations reveals that anthropogenic influence has increased the likelihood of 2024-like compound events under the current human-induced warming level, with GHG emissions alone amplifying the risk more than 8-fold. Projections suggest that by the end of the 21st century, the recurrence risk of such compound events could rise nearly 10-fold, underscoring their increasing inevitability under continued warming. In contrast, estimates derived from both the parametric GEV–t-copula framework and the nonparametric empirical CDF–t-copula approach consistently indicate a substantial anthropogenic amplification of compound extreme risk over NWCA. However, empirical estimates exhibit considerably wider uncertainty ranges (Table S7 in Supporting Information S1). In particular, empirical co-occurrence RRs are approximately 1.5 times larger than those based on GEV under individual GHG forcing during 2025–2049, but decrease by about 6–7 in magnitude relative to GEV-based estimates during 2050–2074 and 2075–2099. These comparisons suggest that while both methods yield broadly consistent conclusions, parametric GEV-based modeling is preferable when more constrained uncertainty estimates are required. Additionally, these results also remain robust under ALL forcings when an additional 10 CanESM5 ensemble members (r11–r20i1p1f1) are included, suggesting that the attribution conclusions are largely insensitive to the ensemble size of individual models (Table S8 in Supporting Information S1). In addition,

we retained complementary estimates of the occurrence probability and RRs for 2024-like events defined using fixed NWCA area-averaged Rx3day and Tx7day (Table S9 in Supporting Information S1). Although future projections indicate substantially lower occurrence probabilities of individual Rx3day, Tx7day, and compound wet–heat events compared to estimates based on sliding boxes, the associated RRs are higher. During the near-future period (2025–2049), the RR of 2024-like compound extremes rise to 4.86 (90% CI: 2.75–12.35) under ALL forcings, with GHG forcing alone contributing a markedly stronger amplification (RR = 23.86, 90% CI: 14.17–57.33), while this amplification intensifies further in the far-future period, with RRs increasing to 12.22 (90% CI: 7.17–26.50) and 33.11 (90% CI: 20.40–71.79) under ALL and GHG forcings, respectively.

Beyond external forcing, reconstruction of extreme indices based on internal variability expressed via SST highlights the role of specific large-scale ocean–atmosphere patterns. The leading SST mode associated with detrended Rx3day variability features a developing Atlantic SST dipole from winter to March with midlatitude cooling flanked by subtropical and high-latitude warming, together with basin-wide Indian Ocean warming closely linked to ENSO. These SST anomalies drive anomalous low pressure over Europe and high pressure over Siberia, strengthening the southwesterly jet over NWCA and enhancing zonal moisture transport from the Atlantic, thereby favoring extreme precipitation. In contrast, the enhanced high-pressure anomalies favoring Tx7day are primarily modulated by a decaying La Niña tendency, leading to anomalous subsidence over NWCA, increasing surface solar radiation and promoting persistent heatwaves. Statistical reconstruction based on the first SST mode indicates that, for 2024, the SST-related internal variability accounted for 31% and 68% of the Rx3day and Tx7day, respectively, while an additional 17% and 8% contributed from long-term warming. These findings highlight that internal climate variability acts as a non-negligible driver, accompanied by externally forced warming amplifying compound extremes over NWCA. Notably, a portion of the residual variance could not be captured by the reconstruction, likely reflecting local land–atmosphere thermodynamic feedback interactions that are not fully captured by large-scale SST modes. For instance, on intra-seasonal timescales, soil moisture variability and the associated feedbacks in sensible heat and net longwave radiation can amplify near-surface air temperature fluctuations, thereby intensifying extreme heat events (Lim et al., 2025; Y.-N. Wang et al., 2024). In addition, on inter-decadal timescales, the leading SST mode favorable for Tx7day is significantly modulated by the PDO ($p < 0.01$), underscoring the role of low-frequency Pacific variability in shaping regional climate changes.

Overall, our study identifies the dominant modes of synchronous SST anomalies across equatorial and mid-latitude basins that modulate March precipitation and subsequent April heatwaves in NWCA, accompanied by the local soil moisture-temperature feedbacks. Importantly, these SST modes emerge in the preceding winter. For instance, enhanced westerly moisture transport patterns into NWCA associated with increased Rx3day are primarily governed by an Atlantic SST tripole that persists from January to February into early spring. By contrast, a decaying La Niña tendency in the central–eastern equatorial Pacific dominantly leads to anomalous high-pressure anomalies over the NWCA, thereby amplifying Tx7day anomalies. Owing to their slow evolution, these large-scale SST configurations can be monitored several months in advance and incorporated into seasonal forecasting systems as boundary forcings or physically interpretable predictor fields, extending predictability beyond the intrinsic limits of short-range weather forecasts. Nevertheless, given the relatively slow adjustment of SSTs, changes in local hydrological conditions also warrant close attention. Rapid soil moisture depletion following extreme precipitation, coupled with persistently elevated soil temperatures, can serve as additional early-warning signals for the occurrence of heatwaves after extreme precipitation. This underscores the importance of jointly considering large-scale oceanic precursors and fast-evolving land–atmosphere processes when assessing the risk of compound precipitation–heatwave events. However, the relative contributions of individual ocean basins remain to be quantitatively constrained. Future work should disentangle teleconnections from the tropical Pacific, Indian Ocean, and North Atlantic, and assess how their interactions amplify or dampen local wet–heat sequences. For example, North Atlantic SST anomalies have already been shown to enhance the predictability of extreme heat days in CA (Yao, Li, et al., 2024). Advancing the understanding of SST–circulation linkages will further strengthen seasonal forecasting of high-impact events and support climate-resilient agricultural planning and early-warning strategies in this vulnerable region (Jiang et al., 2020; Liu et al., 2025).

Additionally, previous studies have shown that robust attribution of rare extreme events may require ensembles substantially larger than those typically available in DAMIP, in some cases reaching thousands of realizations (Gillett et al., 2025; Schaller et al., 2014). To mitigate this sampling limitation, several complementary strategies have been proposed, including pooling model years beyond the specific event window, combining multiple

climate model ensembles, and increasing sample sizes using statistical approaches such as extreme value theory (Sippel et al., 2015) or ensemble boosting techniques (King, 2017). At the same time, for regional extremes, CMIP6 models with coarse grid spacing (~150 km) are inherently limited in representing sub-grid scale processes, such as convective clouds, complex topography, and other localized weather phenomena that drive extreme events, often leading to systematic underestimation of extreme intensity. Therefore, future studies would benefit from kilometer-scale simulations, which provide higher-resolution, localized insights into climate change impacts, thereby improving risk assessment and adaptation planning (Engelbrecht et al., 2025). Consequently, our DAMIP-based results should be interpreted primarily as relative metrics of risk amplification under anthropogenic forcing, rather than precise estimates of absolute joint-event frequencies. From a risk management perspective, our findings argue for a shift from single-hazard, frequency-based approaches toward compound- and impact-based frameworks. Although the weaker occurrence probability of compound events in future projections, the sharply increasing risk ratios indicate that such events will become less frequent but substantially more damaging. Effective risk management should therefore emphasize preparedness for high-impact event sequences, incorporate compound-event thresholds into early-warning systems, and explicitly account for cascading risks amplified by anthropogenic warming.

Conflict of Interest

The authors declare no conflicts of interest relevant to this study.

Data Availability Statement

All data supporting the conclusions of this study are publicly available. Observed daily precipitation and temperature data from CPC and MSWEP are obtained from P. Xie et al. (2010) and Beck et al. (2019), respectively. ERA5 reanalysis data are derived from Hersbach et al. (2020). The HadISST, ERSST, and OISST data sets were obtained from Rayner et al. (2003), Huang et al. (2017), and Reynolds et al. (2007), respectively. The DAMIP simulations and projections within the CMIP6 framework are from Gillett et al. (2025). The key codes supporting this study are archived in Zenodo and are publicly available from Yao and Tang (2026).

Acknowledgments
We thank the three anonymous reviewers for their constructive comments, which have helped to improve the clarity and quality of this manuscript. This work was supported by the National Key R&D Program of China (2025YFF0812000) and the National Natural Science Foundation of China (42530606 and 42261144687).

References

Abdi, H. (2010). Partial least squares regression and projection on latent structure regression (PLS Regression). *WIREs Computational Statistics*, *2*(1), 97–106. https://doi.org/10.1002/wics.51

Abid, M. A., Kucharski, F., Molteni, F., Kang, I.-S., Tompkins, A. M., & Almazroui, M. (2021). Separating the Indian and Pacific Ocean impacts on the Euro-Atlantic response to ENSO and its transition from early to late winter. *Journal of Climate*, *34*(4), 1531–1548. https://doi.org/10.1175/JCLI-D-20-0075.1

ACAPS. (2024). ACAPS briefing note: Kazakhstan floods (23 April 2024). Retrieved from https://reliefweb.int/report/kazakhstan/acaps-briefing-note-kazakhstan-floods-23-april-2024

Anna Chernova, C. E. A. C. D. (2024). Floods ravage regions of Russia and Kazakhstan, but worse is yet to come. Retrieved from https://edition.cnn.com/2024/04/10/world/russia-kazakhstan-floods-ural-putin-intl/index.html

Beck, H. E., Wood, E. F., Pan, M., Fisher, C. K., Miralles, D. G., van Dijk, A. I. J. M., et al. (2019). MSWEP V2 Global 3-Hourly 0.1° precipitation: Methodology and quantitative assessment [Dataset]. *Bulletin of the American Meteorological Society*, *100*(3), 473–500. https://doi.org/10.1175/BAMS-D-17-0138.1

Blum, M. F., Feng, Y., Tuholske, C. P., Kim, B., McAdams DeMarco, M. A., Astor, B. C., & Grams, M. E. (2024). Extreme humid-heat exposure and mortality among patients receiving dialysis. *American Journal of Kidney Diseases*, *84*(5), 582–592.e581. NLM. https://doi.org/10.1053/j.ajkd.2024.04.010

Chen, M., Shi, W., Xie, P., Silva, V. B., Kousky, V. E., Wayne Higgins, R., & Janowiak, J. E. (2008). Assessing objective techniques for gauge-based analyses of global daily precipitation. *Journal of Geophysical Research*, *113*(D4). https://doi.org/10.1029/2007jd009132

Dong, X., Zeng, G., Zhang, G., & Yang, X. (2023). Current AMO mitigating extreme high temperatures in Central Asia under global warming. *International Journal of Climatology*, *43*(9), 3947–3962. https://doi.org/10.1002/joc.8066

Du, Y., Xie, S.-P., Huang, G., & Hu, K. (2009). Role of air–sea interaction in the long persistence of El Niño–induced North Indian Ocean warming. *Journal of Climate*, *22*(8), 2023–2038. https://doi.org/10.1175/2008JCLI2590.1

Engelbrecht, F. A., Steinkopf, J., Chang, N., Biskop, S., Malherbe, J., Engelbrecht, C. J., et al. (2025). Extreme event attribution using km-scale simulations reveals the pronounced role of climate change in the Durban floods. *Communications Earth & Environment*, *6*(1), 506. https://doi.org/10.1038/s43247-025-02460-5

Fallah, B., Didovets, I., Rostami, M., & Hamidi, M. (2024). Climate change impacts on Central Asia: Trends, extremes and future projections. *International Journal of Climatology*, *44*(10), 1–23. https://doi.org/10.1002/joc.8519

Fallah, B., Russo, E., Menz, C., Hoffmann, P., Didovets, I., & Hattermann, F. F. (2023). Anthropogenic influence on extreme temperature and precipitation in Central Asia. *Scientific Reports*, *13*(1), 6854. https://doi.org/10.1038/s41598-023-33921-6

Feng, F., Zhao, Y., Huang, A., Li, Y., & Zhou, X. (2022). Different seasonal precipitation anomaly patterns in central Asia associated with two types of El Niño during 1891–2016. *Frontiers in Earth Science*, *10*, 771362. https://doi.org/10.3389/feart.2022.771362

Fischer, E. M., & Knutti, R. (2015). Anthropogenic contribution to global occurrence of heavy-precipitation and high-temperature extremes. *Nature Climate Change*, *5*(6), 560–564. https://doi.org/10.1038/nclimate2617

Gillett, N. P., Simpson, I. R., Hegerl, G., Knutti, R., Mitchell, D., Ribes, A., et al. (2025). The detection and attribution model intercomparison project (DAMIP v2.0) contribution to CMIP7 [Dataset]. *Geoscientific Model Development*, *18*(14), 4399–4416. https://doi.org/10.5194/gmd-18-4399-2025

Guglielmi, G. (2022). Climate change is turning more of Central Asia into desert. *Nature*. https://doi.org/10.1038/d41586-022-01667-2

Hawkins, E., & Sutton, R. (2011). The potential to narrow uncertainty in projections of regional precipitation change. *Climate Dynamics*, *37*(1–2), 407–418. https://doi.org/10.1007/s00382-010-0810-6

Hersbach, H., Bell, B., Berrisford, P., Hirahara, S., Horányi, A., Muñoz-Sabater, J., et al. (2020). The ERA5 global reanalysis [Dataset]. *Quarterly Journal of the Royal Meteorological Society*, *146*(730), 1999–2049. https://doi.org/10.1002/qj.3803

Hu, K., Liu, Y., Huang, G., He, Z., & Long, S.-M. (2020). Contributions to the interannual summer rainfall variability in the mountainous area of Central China and their decadal changes. *Advances in Atmospheric Sciences*, *37*(3), 259–268. https://doi.org/10.1007/s00376-019-9099-5

Huang, B., Thorne, P. W., Banzon, V. F., Boyer, T., Chepurin, G., Lawrimore, J. H., et al. (2017). Extended reconstructed sea surface temperature, version 5 (ERSSTv5): Upgrades, validations, and intercomparisons [Dataset]. *Journal of Climate*, *30*(20), 8179–8205. https://doi.org/10.1175/JCLI-D-16-0836.1

Ito, R., Imada, Y., & Kawase, H. (2023). Regional characteristics of attribution risk on the record-high-temperature event of 2022 rainy season in Japan. *Bulletin of the American Meteorological Society*, *104*(11), E2121–E2126. https://doi.org/10.1175/BAMS-D-23-0172.1

Jiang, J., & Zhou, T. (2021). Human-induced rainfall reduction in drought-prone Northern Central Asia. *Geophysical Research Letters*, *48*(7), e2020GL092156. https://doi.org/10.1029/2020gl092156

Jiang, J., Zhou, T., Chen, X., & Wu, B. (2021). Central Asian precipitation shaped by the tropical Pacific decadal variability and the Atlantic multidecadal variability. *Journal of Climate*, *34*(18), 7541–7553. https://doi.org/10.1175/jcli-d-20-0905.1

Jiang, J., Zhou, T., Wang, H., Qian, Y., Noone, D., & Man, W. (2020). Tracking moisture sources of precipitation over Central Asia: A study based on the water-source-tagging method. *Journal of Climate*, *33*(23), 10339–10355. https://doi.org/10.1175/jcli-d-20-0169.1

King, A. D. (2017). Attributing changing rates of temperature record breaking to anthropogenic influences. *Earth's Future*, *5*(11), 1156–1168. https://doi.org/10.1002/2017EF000611

Künsch, H. (1993). The jackknife and the bootstrap for general stationary observations. *Annals of Statistics*, *17*(3). https://doi.org/10.1214/aos/1176347265

Kurishbaev, A., Amanzholova, R., Adenova, D., Sagin, J., Burlibayeva, D., Sarsekova, D., et al. (2024). Comparative assessment of the mountainous river basin in Kyrgyz-Kazakh region of Central Asia with River Basins in Australia, Canada and USA. *Grassroots Journal of Natural Resources*, *7*(1), 99–122. https://doi.org/10.33002/nr2581.6853.070106

Li, W., Jiang, Z., & Li, L. (2023). Anthropogenic influence on the record-breaking compound hot and dry event in summer 2022 in the Yangtze River Basin in China. *Bulletin of the American Meteorological Society*, *104*(11), E1928–E1934. https://doi.org/10.1175/bams-d-23-0149.1

Liang, C., Yuan, J., Tang, X., Kan, H., Cai, W., & Chen, J. (2024). The influence of humid heat on morbidity of megacity Shanghai in China. *Environment International*, *183*, 108424. https://doi.org/10.1016/j.envint.2024.108424

Lim, Y., Molod, A. M., Koster, R. D., & Santanello, J. A. (2025). The role of land–atmosphere coupling in subseasonal surface air temperature prediction across the contiguous United States. *Hydrology and Earth System Sciences*, *29*(15), 3435–3445. https://doi.org/10.5194/hess-29-3435-2025

Lioubimtseva, E., & Henebry, G. M. (2009). Climate and environmental change in arid Central Asia: Impacts, vulnerability, and adaptations. *Journal of Arid Environments*, *73*(11), 963–977. https://doi.org/10.1016/j.jaridenv.2009.04.022

Liu, Z., Jiao, L., & Lian, X. (2025). Changes in compound extreme events and their impacts on cropland productivity in China, 1985–2019. *Earth's Future*, *13*(3), e2024EF005038. https://doi.org/10.1029/2024EF005038

Luo, M., Liu, T., Meng, F., Duan, Y., Bao, A., Frankl, A., & De Maeyer, P. (2019). Spatiotemporal characteristics of future changes in precipitation and temperature in Central Asia. *International Journal of Climatology*, *39*(3), 1571–1588. https://doi.org/10.1002/joc.5901

Meng, L., Zhao, Y., & Li, M. (2021). Effects of whole SST anomaly in the Tropical Indian Ocean on summer rainfall over Central Asia. *Frontiers in Earth Science*, *9–2021*, 738066. https://doi.org/10.3389/feart.2021.738066

Min, S.-K., Jo, S.-Y., Seong, M.-G., Kim, Y.-H., Son, S.-W., Byun, Y.-H., et al. (2022). Human contribution to the 2020 summer successive hot-wet extremes in South Korea. *Bulletin of the American Meteorological Society*, *103*(3), S90–S97. https://doi.org/10.1175/bams-d-21-0144.1

OCHA. (2024). Devastating floods in Kazakhstan: A national emergency. Retrieved from https://reliefweb.int/report/kazakhstan/devastating-floods-kazakhstan-national-emergency

Peng, D., Zhou, T., Zhang, L., & Wu, B. (2018). Human contribution to the increasing summer precipitation in Central Asia from 1961 to 2013. *Journal of Climate*, *31*(19), 8005–8021. https://doi.org/10.1175/JCLI-D-17-0843.1

Peng, D., Zhou, T., Zhang, L., Zhang, W., & Chen, X. (2019). Observationally constrained projection of the reduced intensification of extreme climate events in Central Asia from 0.5°C less global warming. *Climate Dynamics*, *54*(1–2), 543–560. https://doi.org/10.1007/s00382-019-05014-6

Peng, D., Zhou, T., Zhang, L., & Zou, L. (2019). Detecting human influence on the temperature changes in Central Asia. *Climate Dynamics*, *53*(7–8), 4553–4568. https://doi.org/10.1007/s00382-019-04804-2

Raganato, A., Abid, M. A., & Kucharski, F. (2024). The combined link of the Indian Ocean dipole and ENSO with the North Atlantic–European circulation during early boreal winter in reanalysis and the ECMWF SEAS5 hindcast. *Journal of Climate*, *38*(2), 445–460. https://doi.org/10.1175/JCLI-D-23-0703.1

Rahman, M. A., Afridi, S., Hossain, M. B., Rana, M., Al Masum, A., Rahman, M. M., & Al-Maruf, A. (2024). Nexus between heat wave, food security and human health (HFH): Developing a framework for livelihood resilience in Bangladesh. *Environmental Challenges*, *14*, 100802. https://doi.org/10.1016/j.envc.2023.100802

Rayner, N., Parker, D. E., Horton, E., Folland, C. K., Alexander, L. V., Rowell, D., et al. (2003). Global analyses of sea surface temperature, sea ice, and night marine air temperature since the late nineteenth century [Dataset]. *Journal of Geophysical Research*, *108*(D14), 4407. https://doi.org/10.1029/2002JD002670

Ren, Y., Yu, H., Huang, J., Zhou, J., Luo, H., & Cheng, S. (2025). Impact of mid-high latitude circulation and surface thermal forcing on drought events in Central Asia. *Climate Dynamics*, *63*(2), 90. https://doi.org/10.1007/s00382-024-07577-5

Reynolds, R. W., Smith, T. M., Liu, C., Chelton, D. B., Casey, K. S., & Schlax, M. G. (2007). Daily high-resolution-blended analyses for sea surface temperature [Dataset]. *Journal of Climate*, *20*(22), 5473–5496. https://doi.org/10.1175/2007JCLI1824.1

Robinson, A., Lehmann, J., Barriopedro, D., Rahmstorf, S., & Coumou, D. (2021). Increasing heat and rainfall extremes now far outside the historical climate. *npj Climate and Atmospheric Science*, *4*(1), 45. https://doi.org/10.1038/s41612-021-00202-w

Schaller, N., Otto, F., Van Oldenborgh, G. J., Massey, N., Sparrow, S., & Allen, M. (2014). The heavy precipitation event of May–June 2013 in the upper Danube and Elbe basins. *Bulletin of the American Meteorological Society*, *95*, S69–S72.

Sippel, S., Mitchell, D., Black, M. T., Dittus, A. J., Harrington, L., Schaller, N., & Otto, F. E. (2015). Combining large model ensembles with extreme value statistics to improve attribution statements of rare events. *Weather and Climate Extremes*, *9*, 25–35. https://doi.org/10.1016/j.wace.2015.06.004

Smoliak, B. V., Wallace, J. M., Stoelinga, M. T., & Mitchell, T. P. (2010). Application of partial least squares regression to the diagnosis of year-to-year variations in Pacific Northwest snowpack and Atlantic hurricanes. *Geophysical Research Letters*, *37*(3). https://doi.org/10.1029/2009GL041478

Stan, C., Straus, D., Frederiksen, J., Lin, H., Maloney, E., & Schumacher, C. (2017). Review of tropical-extratropical teleconnections on intraseasonal time scales. *Reviews of Geophysics*, *55*(4), 902–937. https://doi.org/10.1002/2016rg000538

Sun, K., Yang, P., Xia, J., Huang, H., Chen, Y., Li, Z., et al. (2025a). Extreme precipitation analysis in Central Asia based on the two-step kappa approach under global change. *Climate Dynamics*, *63*(5), 206. https://doi.org/10.1007/s00382-025-07683-y

Sun, K., Yang, P., Xia, J., Huang, H., Chen, Y., Zhu, Y., et al. (2025b). Spatiotemporal correlations and driving factors of multiple drought in Central Asia. *Atmospheric Research*, *324*, 108199. https://doi.org/10.1016/j.atmosres.2025.108199

Sun, X., Li, S., Hong, X., & Lu, R. (2019). Simulated influence of the Atlantic multidecadal oscillation on summer Eurasian nonuniform warming since the mid-1990s. *Advances in Atmospheric Sciences*, *36*(8), 811–822. https://doi.org/10.1007/s00376-019-8169-z

Tang, H., Huang, G., Hu, K., Wang, J., Huang, C., & Yang, X. (2025). Compound extreme events and health risks in China: A review. *Atmospheric and Oceanic Science Letters*, *18*(5), 100647. https://doi.org/10.1016/j.aosl.2025.100647

Tang, H., Wang, J., Chen, Y., Tett, S. F., Sun, Y., Cheng, L., et al. (2023). Human contribution to the risk of 2021 Northwestern Pacific concurrent marine and terrestrial summer heat. *Bulletin of the American Meteorological Society*, *104*(3), E673–E679. https://doi.org/10.1175/BAMS-D-22-0238.1

Tian, Y., Yan, Z., & Li, Z. (2021). Spatial and temporal variations of extreme precipitation in Central Asia during 1982–2020. *Atmosphere*, *13*(1), 60. https://doi.org/10.3390/atmos13010060

Trenberth, K. E., Fasullo, J. T., & Shepherd, T. G. (2015). Attribution of climate extreme events. *Nature Climate Change*, *5*(8), 725–730. https://doi.org/10.1038/nclimate2657

Umirbekov, A., Peña-Guerrero, M. D., & Müller, D. (2022). Regionalization of climate teleconnections across Central Asian mountains improves the predictability of seasonal precipitation. *Environmental Research Letters*, *17*(5), 055002. https://doi.org/10.1088/1748-9326/ac6229

Wallace, J., Fu, Q., Smoliak, B., Lin, P., & Johanson, C. (2012). Simulated versus observed patterns of warming over the extratropical Northern Hemisphere continents during the cold season. *Proceedings of the National Academy of Sciences of the United States of America*, *109*(36), 14337–14342. https://doi.org/10.1073/pnas.1204875109

Wang, C., Li, Z., Chen, Y., Li, Y., Liu, X., Hou, Y., et al. (2022). Increased compound droughts and heatwaves in a double pack in Central Asia. *Remote Sensing*, *14*(13), 2959. https://doi.org/10.3390/rs14132959

Wang, J., Chen, Y., Nie, J., Yan, Z., Zhai, P., & Feng, J. (2022). On the role of anthropogenic warming and wetting in the July 2021 Henan record-shattering rainfall. *Science Bulletin*, *67*(20), 2055–2059. NLM. https://doi.org/10.1016/j.scib.2022.09.011

Wang, Y.-N., Zuo, Z.-Y., Qiao, L., Zhang, K.-W., Chang, M.-Y., Xiao, D., et al. (2024). Amplification effect of intra-seasonal variability of soil moisture on heat extremes over Eurasia. *Advances in Climate Change Research*, *15*(1), 1–8. https://doi.org/10.1016/j.accre.2024.01.008

Wang, Z., Sun, Y., Zhang, X., Li, T., Li, C., Min, S.-K., & Hu, T. (2023). Human influence on historical heaviest precipitation events in the Yangtze River Valley. *Environmental Research Letters*, *18*(2), 024044. https://doi.org/10.1088/1748-9326/acb563

Wu, R., Kirtman, B. P., & Krishnamurthy, V. (2008). An asymmetric mode of tropical Indian Ocean rainfall variability in boreal spring. *Journal of Geophysical Research*, *113*(D5). https://doi.org/10.1029/2007JD009316

Xie, J., Tang, Q., Golaz, J.-C., & Lin, W. (2024). Record high 2022 September-mean temperature in Western North America. *Bulletin of the American Meteorological Society*, *105*(2), E306–E312. https://doi.org/10.1175/BAMS-D-23-0148.1

Xie, P., Chen, M., & Shi, W. (2010). CPC unified gauge-based analysis of global daily precipitation [Dataset]. In *Preprints, 24th Conference on Hydrology, Atlanta, GA* (Vol. 2). American Meteorological Society. Retrieved from https://ams.confex.com/ams/90annual/webprogram/Paper163676.html

Xie, T., Huang, W., Chang, S., Zheng, F., Chen, J., Chen, J., et al. (2020). Moisture sources of extreme precipitation events in arid Central Asia and their relationship with atmospheric circulation. *International Journal of Climatology*, *41*(S1), E271–E282. https://doi.org/10.1002/joc.6683

Yang, J., Liu, Q., Xie, S.-P., Liu, Z., & Wu, L. (2007). Impact of the Indian Ocean SST basin mode on the Asian summer monsoon. *Geophysical Research Letters*, *34*(2). https://doi.org/10.1029/2006GL028571

Yang, Y., Xie, S.-P., Wu, L., Kosaka, Y., Lau, N.-C., & Vecchi, G. A. (2015). Seasonality and predictability of the Indian Ocean Dipole Mode: ENSO forcing and internal variability. *Journal of Climate*, *28*(20), 8021–8036. https://doi.org/10.1175/JCLI-D-15-0078.1

Yao, M., Li, J., Zheng, C., Yao, M., & Zhu, Z. (2024). How predictable is the anomaly pattern of summer extreme high-temperature days over Central Asia? *Climate Dynamics*, *62*(8), 7651–7664. https://doi.org/10.1007/s00382-024-07299-8

Yao, M., & Tang, H. (2026). Main codes for spring 2024 compound floods in Central Asia [Dataset]. *Zenodo*. https://doi.org/10.5281/zenodo.18604236

Yao, M., Tang, H., & Huang, G. (2025). Roles of external forcing and internal variability in winter precipitation changes over Central Asia. *Earth's Future*, *13*(7), e2025EF006064. https://doi.org/10.1029/2025EF006064

Yao, M., Tang, H., Huang, G., & Wu, R. (2024). Interdecadal shifts of ENSO influences on Spring Central Asian precipitation. *npj Climate and Atmospheric Science*, *7*(1), 194. https://doi.org/10.1038/s41612-024-00742-x

Yu, T., Chen, W., Huang, P., Huang, G., & Yang, X. (2025). Weakened influence of ENSO on the East Asian summer monsoon since the early 2000s. *npj Climate and Atmospheric Science*, *8*(1), 114. https://doi.org/10.1038/s41612-025-00983-4

Zhang, M., Chen, Y., Shen, Y., & Li, Y. (2017). Changes of precipitation extremes in arid Central Asia. *Quaternary International*, *436*, 16–27. https://doi.org/10.1016/j.quaint.2016.12.024

Zhang, W., Li, L., Zhou, T., Brody, M., He, Q., Xu, M., & Madibekov, A. (2025). Central Asian compound flooding in 2024 contributed by climate warming and interannual variability. *Advances in Atmospheric Sciences*, *42*(10), 2195–2202. https://doi.org/10.1007/s00376-025-4425-6

Zhang, W., Li, W., Zhu, L., Ma, Y., Yang, L., Lott, F. C., et al. (2020). Anthropogenic influence on 2018 summer persistent heavy rainfall in central western China. *Bulletin of the American Meteorological Society*, *101*(1), S65–S70. https://doi.org/10.1175/bams-d-19-0147.1

Zhou, T., Ren, L., & Zhang, W. (2021). Anthropogenic influence on extreme Meiyu rainfall in 2020 and its future risk. *Science China Earth Sciences*, *64*(10), 1633–1644. https://doi.org/10.1007/s11430-020-9771-8

Zou, S., Abuduwaili, J., Duan, W., Ding, J., De Maeyer, P., Van De Voorde, T., & Ma, L. (2021). Attribution of changes in the trend and temporal non-uniformity of extreme precipitation events in Central Asia. *Scientific Reports*, *11*(1), 15032. https://doi.org/10.1038/s41598-021-94486-w